Microstructures, phase and mechanical characterisation of Al_2O_3-ZrO_2-TiO_2 coating produced by atmospheric plasma spraying

Cynthia Sin Ting Chang [a,*], Marcus Wyss [b], Michal Andrzejewski [a,c], Geoffrey Darut [d], Lukas Graf [e], Vladimir Novak [a], Margie Olbinado [a,f], Susanne Erpel [b], Alexander Vogel [b], Simon Bode [g], Michael de Wild [e], Armando Salito [h]

[a] ANAXAM, Park Innovarre, Parkstrasse 1, CH-5234 Villigen, Switzerland
[b] Swiss Nanoscience Institute, University of Basel, 4056 Basel, Switzerland
[c] Laboratory for Condensed Matter, Paul Scherrer Institut, Forschungsstrasse 111, CH-5232 Villigen PSI, Switzerland
[d] UTBM, CNRS, ICB, F-90010 Belfort cedex, France
[e] Institute for Medical Engineering and Medical Informatics, School of Life Sciences FHNW Hofackerstrasse 30, CH-4132 Muttenz, Switzerland
[f] Laboratory for Macromolecules and Bioimaging, Paul Scherrer Institut, Forschungsstrasse 111, CH-5232 Villigen PSI, Switzerland
[g] Institute for Photon Science and Synchrotron Radiation, Karlsruhe Institute of Technology, Hermann-von-Helmholtz-Platz 1, D-76344 Eggenstein-Leopoldshafen, Germany
[h] Gulhfi AG, Sonnenweg 15, CH-5610 Wohlen, Switzerland

ARTICLE INFO

ABSTRACT

The microstructure, crystallographic phases, and mechanical properties of a newly developed Al_2O_3 – TiO_2 – ZrO_2 ternary ceramic coating were characterized. The coatings were produced by atmospheric plasma spraying as a preblended powder on Ti-6Al-4 V substrates using the new generation of the Debye-Larmor cascaded plasma torch. The 400 μm thick as-sprayed ternary ceramic coating is compact and neither delamination nor inter-/ trans-granular cracks were found. The coating consists of single phase α-Al_2O_3, monoclinic m-ZrO_2, and a nanocrystalline dual phase structure of α-Al_2O_3 and m-ZrO_2. Ti is either present as $ZrTiO_4$ or as solute in the dual phase. Cracking from the tip of the indent is rare and delamination was not observed after the progressive scratch test. The coating has potential in high wear applications for example in medical devices.

1. Introduction

The metal-on-polymer design is the most common orthopedic implant nowadays [1]. For knee joints, it consists of a metal femoral component and a polymeric tibial component. CoCr alloys have been used for metal components since the sixties [2] and today majority of the artificial joints are made of CoCr-based alloys [3]. However, patients who has received endoprosthetic surgery can lead to sensitization of chromium, cobalt, and nickel [4,5]. The ionic release of the active elements from the implant material and the implant debris can lead to osteolysis and other allergic responses of the host such as eczema, swelling, and sterile [6,7]. Furthermore, debris from articulating joints can lead to wear.

Other metal alloys, for example Ti6Al4 V [8,9] can replace CoCr alloys to avoid sensitization and putting a ceramic coating on the metal alloy can act as a protective layer, to increase the wear resistance and to minimize debris formation from metal-on-polymer sliding [10]. Among the ceramic coatings, metal oxide coatings are one of the frequently used [11]. Metal oxide coatings, such as Alumina Al_2O_3 [12] and Zirconia ZrO_2 [13] are bioinert ceramic coatings which have excellent wear resistance, high oxidation resistance as well as corrosion resistance in extreme conditions [14].

Although ceramic coatings display excellent mechanical properties under compression, those composed of a single component, such as Al_2O_3, are prone to brittleness and poor toughness [15,16]. To overcome this weakness, ceramic coatings based on a mixture of two single-oxide ceramics have been developed in the last 20 years. For example, by mixing Alumina (Al_2O_3) with Titania (TiO_2) the corrosion and wear resistance can be enhanced [17,18]. A similar effect is observed when Zirconia (ZrO_2) is added to Alumina, where the toughness, thermal stability and shock resistance are increased [19,20].

To further improve the properties of the Al_2O_3-ZrO_2 coatings,

---

attempts have been made to combine all three single oxides into a ternary oxide (Al_2O_3-ZrO_2-TiO_2). Al_2O_3 is a hard ceramic, chemically stable and with excellent electrical and corrosion resistance, but with limited mechanical resistance which is prone to brittleness. ZrO_2 is well known as an extremely tough material with very low thermal conductivity and limited hardness. TiO_2 is also known as an acceptable tough material able to ''dissolve in a ceramic matrix'' and fill micropores which reduces the coating porosity and improves the surface machinability which leads to a lower surface roughness. As a result, ternary Al_2O_3-ZrO_2-TiO_2 coatings have a dense microstructure with low porosity and less microcracks when compared to Al_2O_3-ZrO_2 coatings [21]. The thermal shock resistance is also increased when the Al_2O_3-ZrO_2-TiO_2 coating is sprayed on the NiCrAlY bonding layer with a Ti-6Al4-V titanium alloy substrate [22].

To produce ceramic coatings, atmospheric plasma spraying (APS) has been used for more than 30 years [23,24]. It is a highly flexible and efficient technique that can be adapted to pre-existing industrial environments. In addition, the process is considered cost-effective and environmentally friendly. The principle of this technology is to create a high-energy plasma capable of melting the powder material and spraying it onto the surface to be coated [25]. The most common plasma torches are composed of a tungsten cathode shaped by a tip and a copper anode which has a cylindrical geometry [26]. One of the most problematic instabilities of this type of cathode/anode configuration is called the "re-strike instability" [27,28], the root of the arc moves permanently onto the surface of the anode in a back-and-forth movement with a phase of elongation of the arc downstream of the anode, interrupted by a breakdown of the arc which re-bursts upstream or downstream of the previous foot of the arc.

A new generation of plasma torches has appeared in recent years, which specialize in the design of advanced plasma processes [29,30]. Developments have focused on stabilizing the length of the plasma arc and maximizing the arc voltage to allow high power levels while keeping the arc current at a minimum. These new so-called "Debye-Larmor cascaded or segmented anode plasma torches" are characterized by a reduced arc displacement due to the presence of neutrodes between the cathode and the anode [31,32]. These torches use a segmented anode made up of a stack of copper rings isolated from each other (e.g. the "neutrodes") and an anode outlet nozzle on which the arc is fixed. This design also stabilizes the arc as the movement of the arc is limited to the width of the anode ring. The long length of the arc makes it possible to obtain a higher and very stable arc voltage. Also, this new geometry allows the plasma to exist closer to the nozzle outlet (output anode) which improves the efficiency of the torch, and it increases the amount of energy available to treat the particles. Thus, lower power and secondary gas flow rates are required to melt materials and produce coatings. All these advantages result in a lower wear of the electrode and therefore a longer lifetime of the plasma torch.

For certain medical applications where a long-life wear coating resistance is necessary the need for thicker coating (coating thickness > 50 μm) is very important. Thin and hard PVD coating like TiN, TiNbN or ZrN is limited to a coating thickness below 10 μm whose lifetime is dramatically reduced under conditions where scratches by an external body may occur [33,34]. The search for thick anti-wear coating is conditioned by the balance between the hardness and toughness properties of the material. Hard metal oxide complex ceramic applied by plasma spraying may fulfil on one side the anti-wear properties using coating thickness between 50 μm to 500 μm and on the other side the toughness properties required for optimized tribological behavior. On top of that, the plasma spraying process makes it possible to coat small or large surfaces with a certain level of complexity. For example, for medical applications of knee prostheses [11].

In this work, we aim to produce the promising ternary Al_2O_3-ZrO_2-TiO_2 coating with the cascade plasma torch technology by atmospheric plasma spraying. The phases in the coating werefully characterized by synchrotron X-ray diffraction (S-XRD), the microstructure by scanning

Table 1
Basic APS parameters.

Designation	Debye-Larmor T8/O8
Ar/H$_2$ flow rate [SLPM]	50/5
Arc current intensity [A]	500
Power [kW]	60
Spraying distance [mm]	110

electron microscopy (SEM), transmission electron microscopy (TEM) and synchrotron X-ray laminography, and with the first mechanical testing by hardness and scratch tests. From the results, the potential of Al_2O_3-ZrO_2-TiO_2 coating in different applications is shown.

2. Material and methods

A near eutectic Al_2O_3-ZrO_2 composition with an addition of 6% of TiO_2 was chosen as the composition of the starting powder. The ternary ceramic powder was obtained by the fusion of the ceramic raw material based on ZrO_2, Al_2O_3, and TiO_2. Then, to obtain a suitable powder grain size for plasma spraying, the powder was crushed and a particle size distribution between 5 and 45 μm was selected by sieving process. Coatings were manufactured on Ti-6Al-4 V disks with a diameter and thickness of 25.4 mm and 6.3 mm, respectively. Before the spray, they were grit-blasted with F36 corundum with a 2.5 bar pressure to obtain a surface roughness of 3.5 to 5μm. The Debye-Larmor cascaded torch was used for APS and the variations of operating parameters such as current intensity, and argon/hydrogen flow rate are summarized in Table 1. The thickness of the coating, defined as the processing time, was maintained constant across all samples.

Synchrotron X-ray diffraction (S-XRD) was performed on the starting powder and the coating at the Materials Science (MS) beamline at the Swiss Light Source (SLS). A Si standard (NIST 640C) was used to determine the wavelength (1.00133(12) Å) and the NAC ($Na_2Ca_3Al_2F_{14}$) for displacement and zero offset corrections. LaB_6 (NIST SRM 660b) dispersed on the surface of a disc (similar environment to the samples) was used to provide starting point parameters for the peak shape modelling. Samples were collected tilted by 15° with respect to the beam, thus data refinement omitted any reflections for 2θ<15° The samples were rotated with a frequency of 20 Hz, and diffraction patterns were collected using the Mythen III detector with an acquisition time of 30 s.

The microstructures of the powder and the cross-section of the coating were investigated by Scanning Electron Microscopy (SEM). Powders were cold-mounted to epoxy and conductive filler and then mechanically polished to obtain a smooth surface. The cross-section of the coating was polished using an ion beam milling system Leica EM TIC 3X. The polishing was carried out with a voltage of 6 kV and a current of 2.2 mA for 3 h. SEM and backscattered electron (BSE) imaging was carried out with an ESEM XL30 from Philips. The SEM-EDX (Energy Dispersive X-Ray Spectroscopy) line scan of the metal coating sample was carried out at 30 kV using a SDD Apollo XV detector from EDAX. BSE images were taken at 30 kV. For the embedded powder SEM-EDX line scans were carried out at 20 kV and BSE images at 20 kV.

Transmission Electron Microscopy (TEM) was performed to examine the nano-crystalline phases in the coatings. Electron-transparent specimens for TEM investigations were prepared in cross-section with an FEI Helios NanoLab 650 DualBeam focused ion beam (FIB) operated at 30 kV and beam currents between 240 pA and 83 pA. A JEOL JEM-F200 equipped with a cold field-emission gun and operated at 200 kV was used for high-resolution TEM (HRTEM) and Scanning TEM (STEM) imaging in combination with EDX mapping. For HRTEM imaging, a 40 μm objective lens aperture was inserted, while selected-area diffraction patterns (SAED) were obtained using a 10 μm SAED aperture.

Synchrotron Laminography was performed on the coating at ID19 of the European Synchrotron Radiation Facility (ESRF) [35]. The sample
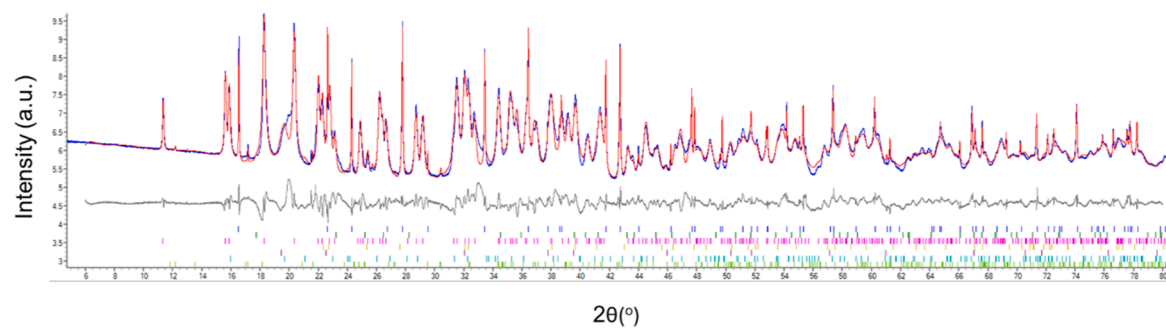
(a)
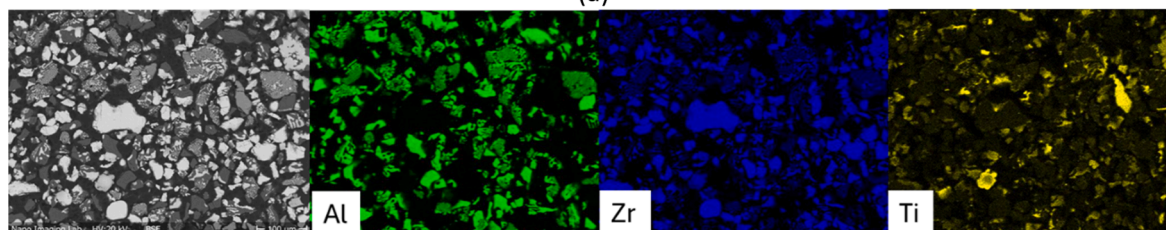
(b)
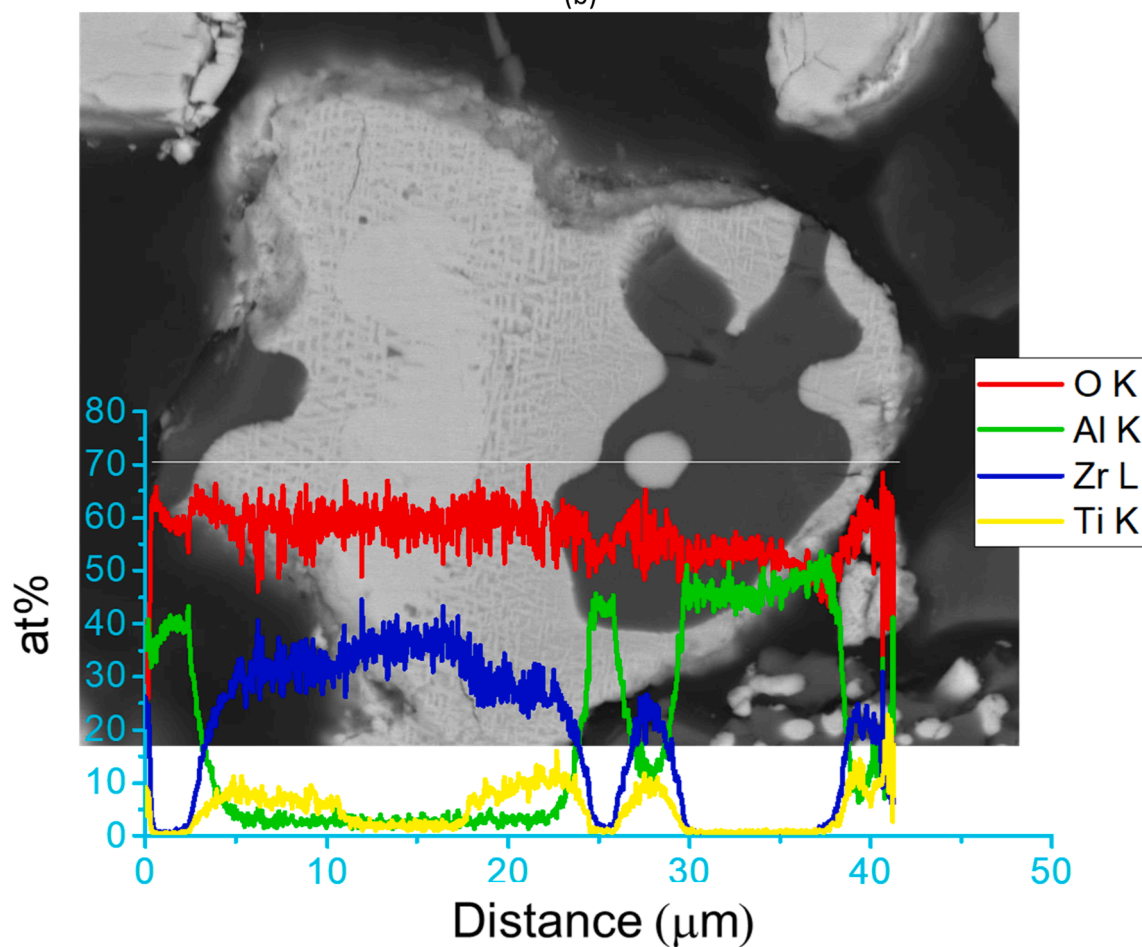
(c)

Fig. 1. (a) XRD result (blue) of the powder. The red curve is the refined result, and the grey curve is the refined residual. The peaks for different phases are fitted accordingly. (b) BSE image of the mechanically polished powder and EDS mapping of the same area showing the Al (green), Zr (blue) and Ti (yellow) content in the powder. (c) EDS line scan of a powder with different phases showing compositional changes of Al, Zr and Ti along the powder.

Table 2
Volume fraction of corresponding phases of powder.

Phases	Volume fraction (%)
Monoclinic m-ZrO$_2$	51.14
Corundum a-Al$_2$O$_3$	41.99
ZrTiO$_4$	4.59
Al$_2$TiO$_5$	0.72
Tetragonal t-ZrO$_2$	0.29
Rutile TiO$_2$	0.12

was placed in the X-ray beam of energy 65 keV and was scanned in a range of 370° with 3701 projections collected. The rotation axis was tilted to 30.168° with respect to the X-ray beam path.

Microhardness and stretch tests were performed on the Al$_2$O$_3$-ZrO$_2$-TiO$_2$ coating. Before conducting microhardness according to DIN EN 843–4: 2005 and scratch tests according to ISO G99: Standard testing parameters for the ball on disc tests, the surface was mechanically polished on a Struers TegraForce-5 system with P1200 SiC wet sanding paper for several hours. Then, microhardness tests were performed normal and parallel to the coating surface. The Vickers hardness measurements HV-1 were conducted on a Struers Duramin 40 system with a dwelling time of t = 10 s according to Vickers DIN EN 843–4:2005. N = 10 indents were made for each coating and the results were averaged. Plasma-sprayed TiO$_2$ coatings served as references for Vickers hardness measurements.

Afterwards, scratch experiments were carried out on the coating surface using a Bruker UMT TriboLab system equipped with a modular force sensor for 2–200 N (DHF-20) and a Rockwell diamond tip (HR-1) with a tip radius of 200 μm. The scratch test was performed with a progressive load from 4 N to 60 N with a force increase of 4 N/mm (resulting in a scratch length of 14 mm) and a scratch speed of 0.073 mm/*sec* (190 s). A total of 5 scratches were created, alternately from right to left and vice versa, each with a spacing of 2.5 mm. The scratches then were investigated by a SEM, Hitachi TM3030. Attention was given to the type of deformation, the base, surrounding and the width of the scratch track. The observed defects were classified according to the following damage features [36]:

- Crack types: Chevron, arc tensile, Hertz cracks or conformal cracking
- Spallation types: Buckling, wedging, recovery, gross spallation.

3. Results and discussions

3.1. As received powder

The S-XRD analysis shows that the major phases of the received powder consist of Corundum (α-Al$_2$O$_3$), monoclinic m-ZrO$_2$ and around 5% of ZrTiO$_4$, Fig. 1(a) and table 2. The as-received powder consists of non-spherical particles ranging from 50 to 100 μm in size, Fig. 1(b). From the BSE image and the EDX mapping, it is apparent that parts of the powder consist of single-phase Al$_2$O$_3$ or ZrO$_2$. In a minor part of the

powder, a high Ti content is detected. Apart from the single-phase area, there are also areas containing a multi-phase composition which shows bright (BSE value larger than 2500) and dark intensity (BSE value less than 1500). The BSE values will be used again in the last sections when analyzing the splat microstructures. A closer look at the particles with multi-phase composition shows that the bright intensity component consists of two phases, Fig. 1(c). A line profile across the zoomed-in image of a particle shows that the bright contrast consists of Zr (blue line) as the major elements and with a minor composition of Ti (cyan) and Al (green). The dark region is mostly Al (green). To summarize, the S-XRD and SEM results show that the powder is a mixture of single-phase powder either of corundum (α-Al$_2$O$_3$) or monoclinic m-ZrO$_2$, and multi-phase powder of Al$_2$O$_3$ + (ZrO$_2$ - ZrTiO$_4$). This distribution of phases in the powder influences the splat composition of the coating.

3.2. Phase analysis of the coatings

S-XRD measurements were performed on 5 coatings with the same spraying conditions, and they all show very similar results, see Fig. 2. The XRD patterns of all 5 samples coincide with each other except for sharp peaks from the corundum α-Al$_2$O$_3$. Since not all corundum peaks appear in the XRD patterns, it is expected that corundum is present in the coating in large quantities and with large grain sizes compared to other present phases. Apart from the sharp α-Al$_2$O$_3$ peaks other peaks are broad which makes refinement becoming difficult. We can still estimate that the major phases present in the coating are, apart from the α-Al$_2$O$_3$, monoclinic m-ZrO$_2$ and with a small fraction of ZrTiO$_4$.

3.3. Microstructures of the coatings

The microstructures of the coating in the cross-section consist of lamellar splats which is a typical microstructure for APS coatings, Fig. 3 (a). The coating is compact, and voids of the size less than 10 μm and micro-cracks growing along the thickness of the several splats can be observed. No through-thickness cracks nor delamination of the coating can be seen.

Like the powder, a distinct contrast between different phases can be seen in the BSE images. There are splats which have a bright intensity with a BSE value larger than 2200, dark intensity with a BSE value smaller than 1500 and grey intensity which have BSE values in between. From the EDS line scans along the thickness of the coating, the content of O, Al, Zr, Ti and the corresponding BSE values of the splats are listed in Fig. 3(b). Matching with the S-XRD results, the Al and Zr content in the splats and the BSE values from the as-received powder, the splats with BSE values <1500 and high Al content are expected to be α-Al$_2$O$_3$, while the splats with BSE values > 2200 and high Zr content are m-ZrO$_2$. For the splats which have a BSE value between 1500 and 2200, there is not a fixed Al and Zr content in the splats. We define them as "other phases".

The different BSE values of the pores and phases were defined and image segmentation was performed in which the area% of the pores and phases was calculated, Fig. 3(c). The area% of the pores is around 1%
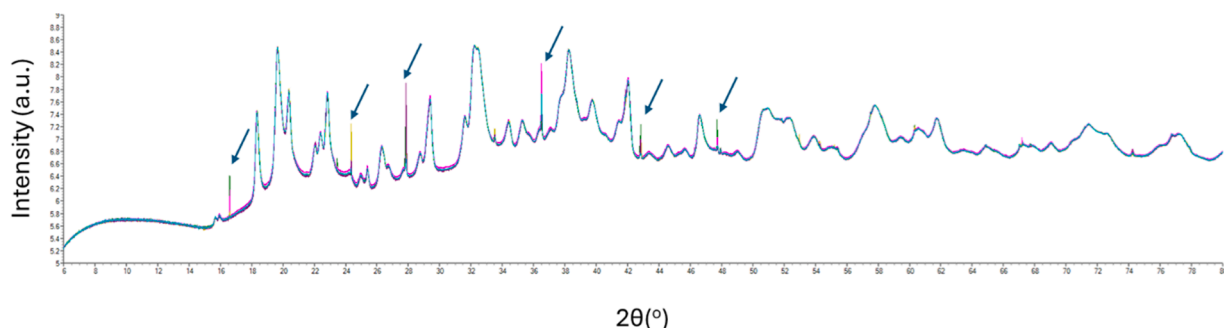

Fig. 2. XRD patterns of 5 coated samples, arrows indicating of the sharp corundum α-Al$_2$O$_3$ peaks.

(a)

(b)

O	Al	Zr	Ti	BSE
57.7	10.1	29.6	2.6	1969
57.8	32.1	8.1	2.0	1067
62.8	11.7	16.0	9.5	2377
58.7	34.4	5.1	1.8	1068
60.1	15.7	14.1	10.2	1795
63.1	5.6	28.7	2.7	2644
62.2	4.4	31.2	2.2	2707
56.4	35.5	7.0	1.1	1108
61.6	18.5	17.6	2.2	2137
56.6	32.9	9.2	1.4	934
58.5	34.8	5.6	1.1	1232
63.3	13.5	21.4	1.7	2759
61.8	27.4	9.5	1.3	1426
62.1	17.2	19.2	1.5	2678
58.8	30.9	9.0	1.3	1066
64.5	18.4	14.9	2.2	2316
59.4	31.4	7.7	1.5	878
61.4	9.9	27.1	1.6	2718
59.7	25.7	12.1	2.5	1614

(c)

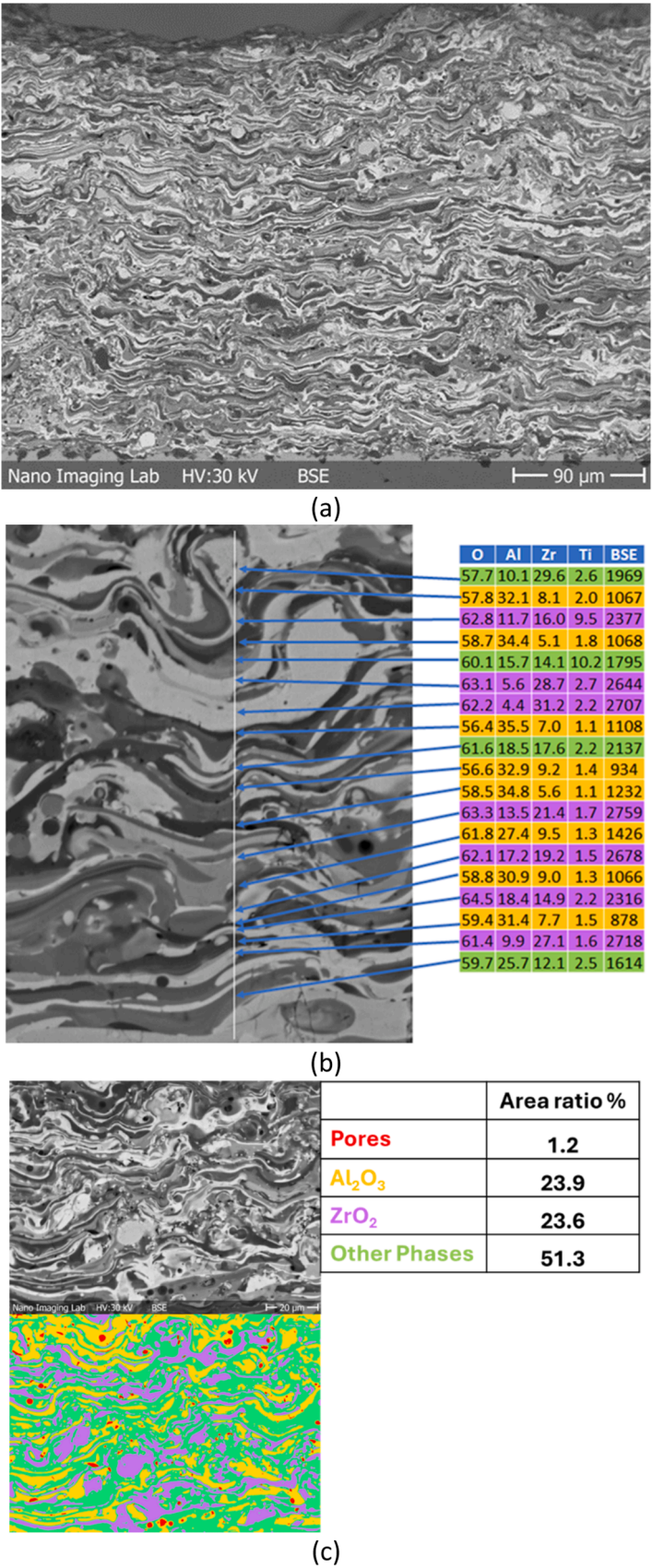|	Area ratio %
Pores	1.2
Al_2O_3	23.9
ZrO_2	23.6
Other Phases	51.3

Fig. 3. (a) BSE image of the cross-section of the coating showing lamellar structure. (b) O, Al Zr and Ti contents and its corresponding BSE contrast of individual splat. (c) Image segmentation and area ratio of the pores, Corundum α-Al_2O_3, Zirconia m-ZrO_2 and the "other" phases.
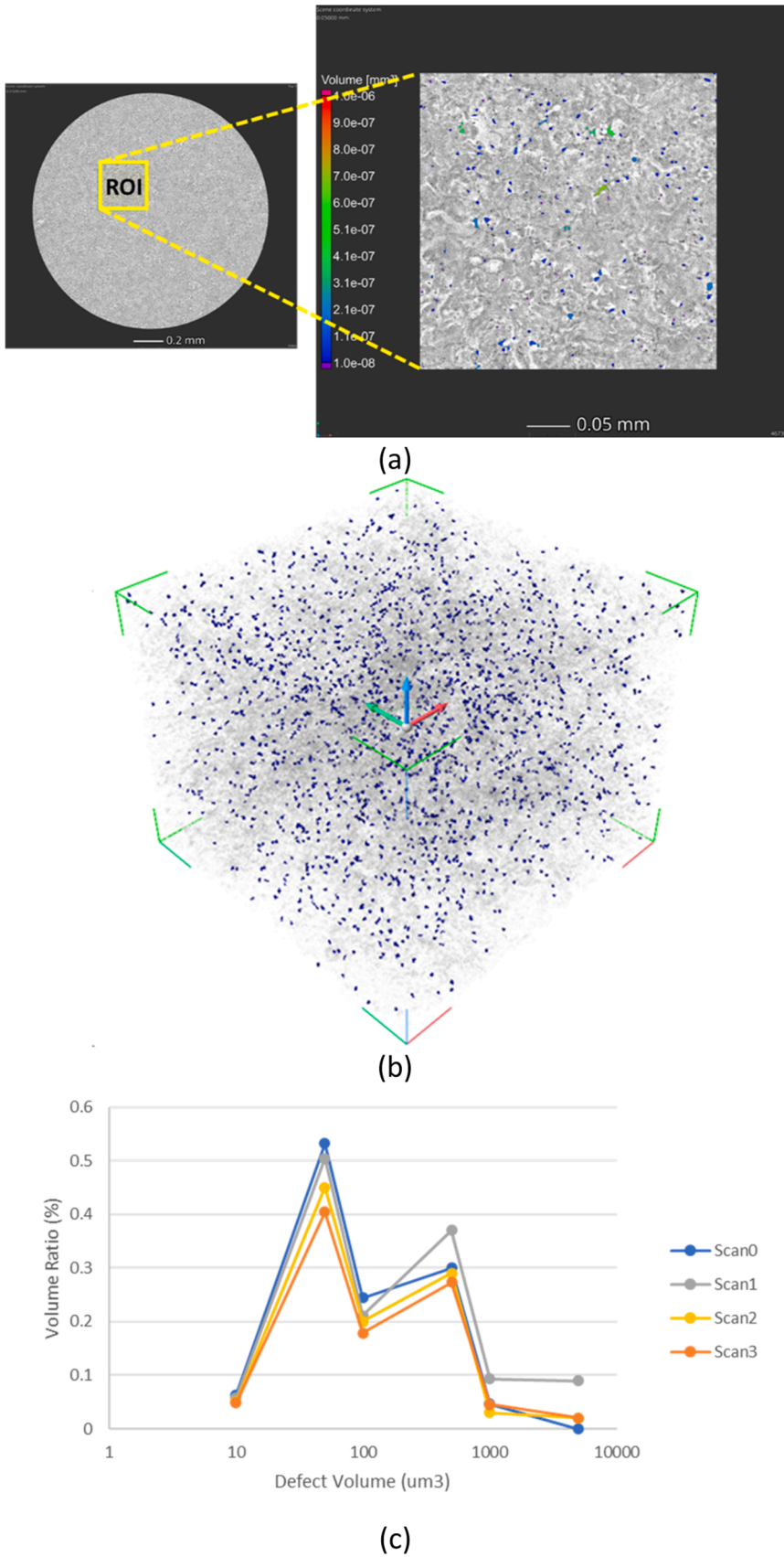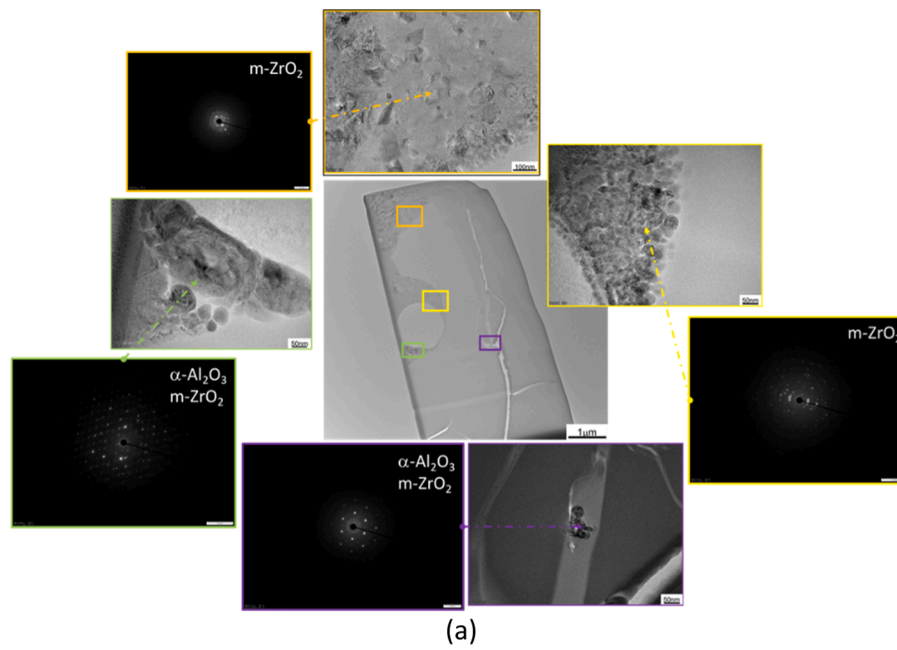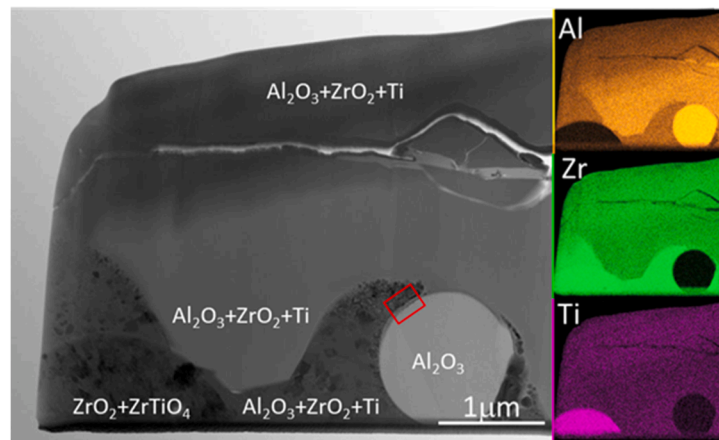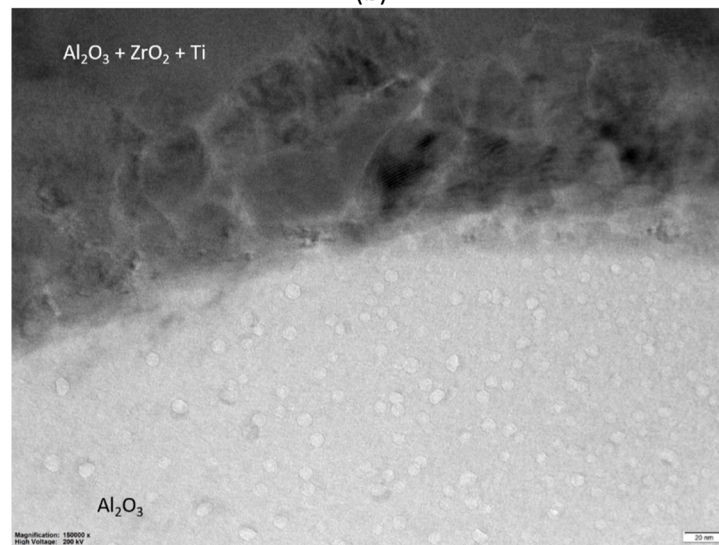
(a)

(b)

(c)

Fig. 4. (a) Transverse cross-section of the coating and the ROI of where the porosity analysis was carried out. (b) The analysed volume of $0.325{\times}0.325{\times}0.260$ mm^3 showing the pores with the size of 1×10^{-8}mm^3 to 0.8×10^{-8}mm^3. (c) Graphs of volume ratio against size of the pores within the ROI.

Fig. 5. (a) HRTEM image of one of the lamellae investigated. Selected Area Diffraction (SAD) and zoom HRTEM images of different area in the overview image showing α-Al_2O_3 and m-ZrO_2 phases present. (b) BF-STEM image and EDX mapping of the area shown in (rotated 90° CCW) (a) and summarizing phases and elements found. (c) HRTEM image shows the depicted area.

from the SEM results, while the area% of α-Al$_2$O$_3$ and m-ZrO$_2$ are both around 24%.

The area ratio from the SEM results gives a rough idea of the porosity information of the coating. For a more quantitative investigation, laminography [37,38] was performed due to the flat, coin-like shape of the sample coating on the Ti-6Al-4V-substrate. Laminography is particularly well suited for 3D imaging of flat and laterally extended specimens, even if they vastly exceed the detector field of view and thus allows scanning of selected Region of Interests (ROIs) without dissection of the sample and thereby damaging of the coating. 4 scans were performed from the side to the center of the sample. No delamination of the coating nor horizontal large cracks through the thickness of the coating can be seen. For each scan, a ROI with the size of 0.325 mm x 0.325 mm x 0.260 mm was chosen for performing the porosity analysis, Fig. 4(a). The segmented pores were grouped according to their sizes, Fig. 4(b) shows an example. Then the volume ratio (with respect to the volume of the ROI) against the volume of the pores was plotted and shown in Fig. 4(c). The porosity distribution is similar in the 4 scans and they all have dominant pore sizes in the 1×10^{-8} mm^3 to 0.8×10^{-8} mm^3 range. The total volume ratio of the porosity is around 1%, which matches the SEM results.

3.4. Sub-micron structures of the coating

The "other phases" that we observed in the SEM as splat with grey BSE contrast still needed to be verified. Therefore, we prepared TEM lamellae from selected areas containing the grey splats. In total, 4 lamellae were investigated by TEM and Fig. 5(a) shows a HRTEM image of one of the lamellae. Selected Area Electron Diffraction (SAED) was performed in different areas, Fig. 5(a) and higher magnification images reveal a complex structure with a size of 50–100 nm. In many areas, multiple diffraction patterns of different orientations overlap with each other. The diffraction patterns were analyzed using the crystallographic tool box CrysTbox [39], and the phases present were identified as α-Al$_2$O$_3$ and m-ZrO$_2$. Ti-containing phases such as TiO$_2$ could not be identified in any diffraction patterns, even though their presence is confirmed by STEM-EDX, Fig. 5(b). Different Al and Zr content is observed in the EDX mapping. We conclude that the "other phases", identified as grey splats, consist of dual phases of α-Al$_2$O$_3$ and m-ZrO$_2$. From the EDX results, the α-Al$_2$O$_3$ content in the splats varies from 15% to 78% while for ZrO$_2$ it varies from 43% to 79%. Ti is always associated in the dual phase with content of 1% to 5%. We cannot identify any ZrTiO$_4$ from the diffraction pattern. However, higher Ti content (over 10%) is found in some splats together with the m-ZrO$_2$. The nano-crystalline dual phase aside, the HRTEM image in Fig. 5(c) shows small structures with a diameter of roughly 5 nm within the bright α-Al$_2$O$_3$ phase. Furthermore, the dark upper section indicates that the dual phase is not homogeneous, either.

The work on ternary Al$_2$O$_3$-ZrO$_2$-TiO$_2$ APS coating is rare. Gao et al. [21]. investigated the effect of the addition of TiO$_2$ on the Al$_2$O$_3$-ZrO$_2$ APS coatings. The ratio of Al$_2$O$_3$/ZrO$_2$ they used was 60:40, which had a hypoeutectic composition [40]. Gao et al. observed a similar microstructure with distinguished BSE contrast for the ZrO$_2$, Al$_2$O$_3$, and mixed-phase splats, that the latter could correspond to the dual-phase of Al$_2$O$_3$-ZrO$_2$ we observe. While they founded α-Al$_2$O$_3$, γ-Al$_2$O$_3$ and t-ZrO$_2$ in the coating, our S-XRD and TEM results show that α-Al$_2$O$_3$ and m-ZrO$_2$ are the major phases. We have only found 0.29% t-ZrO$_2$ in the powder but not in the coating.

The near eutectic composition of our powder consists of a mixture of single-phase α-Al$_2$O$_3$, single-phase m-ZrO$_2$, and multi-phase of Al$_2$O$_3$+(ZrO$_2$- ZrTiO$_4$). Depending on the Al$_2$O$_3$/ZrO$_2$ ratio in the powder, the composition changes from hypo-eutectic, eutectic and hyper-eutectic composition of Al$_2$O$_3$-ZrO$_2$, and therefore the multi-phase powder has a varied ratio of Al$_2$O$_3$/(ZrO$_2$- ZrTiO$_4$). Since APS is a fast heating and cooling process, atomic diffusion is restricted during the APS process. Thus, the sprayed splats resemble the composition of

Table 3
Results of Microhardness tests for Al$_2$O$_3$-ZrO$_2$-TiO$_2$ and TiO$_2$ coatings.

Al$_2$O$_3$-ZrO$_2$-TiO$_2$	Mean [HV 1]	SD [HV 1]	Min [HV 1]	Max [HV 1]
Sample_normal_1 (n = 10)	784.3	56.3	682.9	849.2
Sample_normal_2 (n = 10)	802.5	33.1	760.7	855.8
Sample_parallel_3 (n = 10)	795.7	36.4	736.9	860.6
Average	794.2	42.0	726.8	855.2
TiO$_2$	618	21	654	587

the as-received powder, which also consists of single phase α-Al$_2$O$_3$, single phase m-ZrO$_2$, and nano-crystalline multi-phases of Al$_2$O$_3$+ZrO$_2$. The restricted atomic diffusion also restricts grain growth, especially in the multi-phase Al$_2$O$_3$+ZrO$_2$ splat.

3.5. Mechanical properties of the coating

The pyramidal Vickers impressions with a square shape are all deemed valid according to the DIN EN 843–4: 2005 standard, exhibiting no unacceptable impression phenomena such as cracks at the tips, chipping, curved edges, asymmetries, chipped edges, distortions at the tips, or emerging pores, which are excluded in the DIN EN 843–4: 2005 standard. The microhardness measurements are shown in Table 3. The in-layer parallel tests of sample 3 show comparable results to the normal tests of samples 1 and 2. The microhardness tests of all samples result in a hardness value of 794.2 ± 42.0 HV which is significantly higher than the hardness of 618 ± 21 HV in classical plasma-sprayed TiO$_2$ coatings.

The scratch test results show visible plastic deformation from the start with a normal load of 4 N until the end with 60 N. As expected, the width of the scratch increases with the load. There is no delamination observed in any scratch. The coating is guaranteed to retain its integrity under the specified test conditions. The scratches are shown in Fig. 6(a). The identification of cracks/defects induced by the scratch testing turn out to be challenging since the multiple phases of the ceramic coating led to individual contrast in BSE images, Fig. 6(b). Only very few micro-cracks are observed at regions with higher loads. Within the scratch track, only single arc tensile cracks are identified, see Fig. 6(c) lower left.

Along the entire scratch trajectory from 4 N to 60 N, an impression with increasing width and depth is discernible in all samples. This is remarkable for a ceramic material, indicating a high degree of ductility within the ceramic coating. Material from the coating was displaced laterally, leaving a smooth base. With increasing normal force, particularly at the end of the scratch at 60 N, lateral spalling of the 'recovery spallation' type can be observed and probably resulted in some individual abrasion particles. In contrast, no 'gross spallation' or delamination occurred, indicating good adhesion between the substrate and the coating.

Despite the locally applied loads significantly exceeding any realistic load no crack formation is observed in any sample. Only at the very end of the scratch where loads of 60 N were applied, a single crack shorter than 30 μm, not exceeding 1/3 of the crack width, is observed away from the direction of the scratch. In the regions of the scratch track subjected to the highest normal loads, only isolated instances of single arc tensile cracking are observed.

Goa et al. [21] claimed that the tribological performance, such as the fracture toughness, the adhesive strength and the wear resistance of the Al$_2$O$_3$-ZrO$_2$-TiO$_2$ coating was improved compared to the binary Al$_2$O$_3$-ZrO$_2$ coating, because the addition of TiO$_2$ increase the density and reduce microcracks in the coating. Indeed, literature has shown that the addition of ~ 5% of TiO$_2$ in ZrO$_2$ [41] or ATZ [42] could effectively increase the density of the ceramics, but the increase in the fracture toughness and the wear resistance of the Al$_2$O$_3$-ZrO$_2$-TiO$_2$ coating should be related to the relatively nano-structured ductile phases that
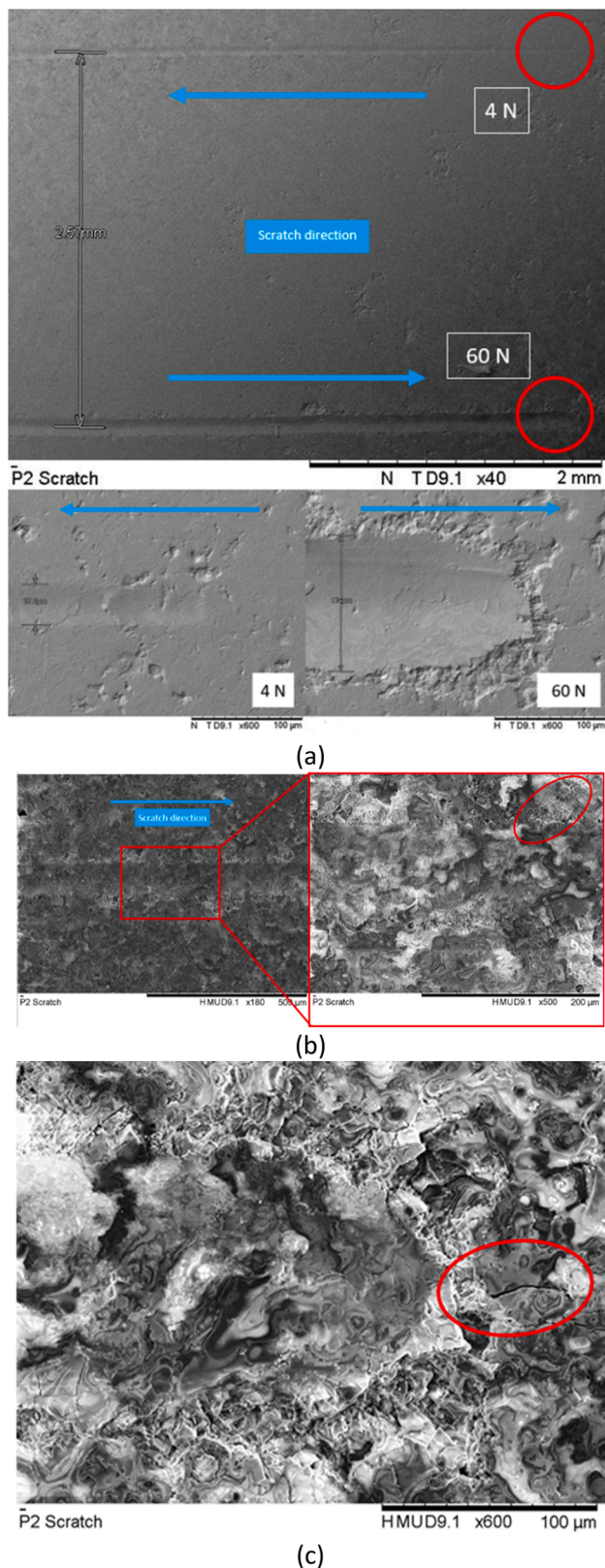
Fig. 6. (a). SEM TOPO image of scratches with increasing normal force from 4 N to 60 N. The scratch directions are indicated with by blue arrows. Plastic deformation is visible from the start until the end (red circles), breakouts at are visible at higher values. (b) BSE images with heavy contrast on the phases of the ceramic coating. With increased load there was some small crack formation and chipping visible. (c) BSE Image of the end of a scratch (60 N) with visible cracks and chipping.

are present, in which plastic deformation is observed after scratch test and tip cracking after indentation is not observed. The ductile phases also can accommodate better the residual stresses that are retained after APS and therefore reducing microcracks.

4. Conclusions

Al_2O_3-ZrO_2-TiO_2 coatings were thermally sprayed on Ti-6Al-4 V substrates using the Debye-Larmor cascaded plasma torch. The ternary ceramic coating is compact with no delamination nor trans-granular cracks. The pore fraction is around 1%. The coating has a typical lamella microstructure with a single phase α-Al_2O_3, m-ZrO_2, and a dual phase of varying content of Al_2O_3 and ZrO_2. Ti is present either in $ZrTiO_4$ or as solute in the dual phase. The coating shows adequate mechanical properties with a high degree of ductility and simultaneously suitable hardness of 794 $\pm$ 42 HV. The progressive scratch tests show plastic deformation but no delamination or spallation indicating good adhesion between the substrate and the coating. Within the scratch track, only single arc tensile cracks are identified at regions with higher loads.

Our thick coating is compact without delamination from the substrate nor from the splats, and no through-thickness crack is observed in SEM cross-sections. Porosity and micro-cracks are at low levels. The formation of the splat-like structure is a direct result of the deposition mechanism, signifying the deposition of individual droplets, which ultimately results in the coating. Thanks to the Debye-Larmor cascade plasma torch technology which stabilizes the heat treatment of the powders to splats, and with the complex nano-size multi-phase system, the coating provides high hardness and high adhesion, while enabling local plastic deformation due to increased ductility. Consequently, the occurrence of adhesion failure or crack initiation is diminished. The coating is suitable for different types of applications, particularly for medical devices which could require long-life high wear resistance and fracture toughness. The next step is to perform further tribological testing like the pin on disk with different combinations of materials like PE or ceramic versus ceramic coating.

CRediT authorship contribution statement

Cynthia Sin Ting Chang: Writing – original draft, Visualization, Validation, Project administration, Methodology, Investigation, Funding acquisition, Data curation, Conceptualization. **Marcus Wyss:** Writing – review & editing, Visualization, Methodology, Investigation, Formal analysis, Data curation. **Michal Andrzejewski:** Validation, Investigation, Formal analysis, Data curation. **Geoffrey Darut:** Writing – review & editing, Validation, Methodology, Investigation. **Lukas Graf:** Validation, Methodology, Formal analysis, Data curation. **Vladimir Novak:** Validation, Project administration, Methodology. **Margie Olbinado:** Writing – review & editing, Visualization, Validation, Methodology, Investigation, Formal analysis. **Susanne Erpel:** Visualization, Methodology, Investigation. **Alexander Vogel:** Writing – review & editing, Visualization, Validation, Formal analysis. **Simon Bode:** Writing – review & editing, Validation, Methodology, Investigation. **Michael de Wild:** Writing – review & editing, Validation, Supervision, Methodology, Formal analysis, Conceptualization. **Armando Salito:** Writing – review & editing, Writing – original draft, Visualization, Validation, Resources, Investigation, Funding acquisition, Conceptualization.

Declaration of competing interest

The authors declare that they have no known competing financial interests or personal relationships that could have appeared to influence the work reported in this paper.

Acknowledgment

References

[1] N.J. Hallab, J.J. Jacobs, Orthopedic applications, in: W.R. Wagner, S.E. Sakiyama-Elbert, G. Zhang, M.J. Yaszemski (Eds.), Biomaterials Science: An Introduction to Materials in Medicine, Elsevier Inc., 2020, pp. 1079–1118.

[2] R.M. Streicher, Tribology of artificial joints, in: E.W. Morscher (Ed.), Endoprosthetics, Springer, Berlin, Heidelberg, 1995, pp. 34–48.

[3] M. Niinomi, Co-Cr-based alloys, in: C. Wen (Ed.), Structural Biomaterials, Woodhear Publishing, 2021, pp. 103–126.

[4] T. Schäfer, E. Böhler, S. Ruhdorfer, L. Weigl, D. Wessner, B. Filipiak, H. E. Wichmann, J. Ring, Epidemiology of contact allergy in adults, Allergy 56 (2001) 1192–1196, https://doi.org/10.1034/j.1398-9995.2001.00086.x.

[5] G. Szczęsny, M. Kopec, D.J. Politis, Z.L. Kowalewski, A. Łazarski, T. Szolc, A review on biomaterials for orthopaedic surgery and traumatology: from past to present, Materials (Basel) 15 (2022) 3622–3632, https://doi.org/10.3390/ma15103622.

[6] D. Guenther, P. Thomas, D. Kendoff, M. Omar, T. Gehrke, C. Haasper, Allergic reactions in arthroplasty: myth or serious problem? Int. Orthop. 40 (2016) 239–244, https://doi.org/10.1007/s00264-015-3001-6.

[7] M.F. Saccomanno, G. Sircana, G. Masci, G. Cazzato, M. Florio, L. Capasso, M. Passiatore, G. Autore, G. Maccauro, E. Pola, Allergy in total knee replacement surgery: is it a real problem? World J. Orthop. 18 (2019) 63–70, https://doi.org/10.5312/wjo.v10.i2.63.

[8] M.Z. Ibrahim, A.A.D. Sarhan, F. Yusuf, M. Hamdi, Biomedical materials and techniques to improve the tribological, mechanical and biomedical properties of orthopedic implants – a review article, J. Alloys Compd. 714 (2017) 636–667, https://doi.org/10.1016/j.jallcom.2017.04.231.

[9] N. Koju, S. Niraula, B. Fotovvati, Additively manufactured porous Ti6Al4V for bone implants: a review, Metals. (Basel) 12 (2022) 687–721, https://doi.org/10.3390/met12040687.

[10] M.T. Mathew, K. Cheng, Y. Sun, V.A.R. Barao, The progress in tribocorrosion research (2010–21): focused on the orthopedics and dental implants, J. Bio. Tribo. Corros. 9 (2023) 48, https://doi.org/10.1007/s40735-023-00767-4.

[11] M. Montazerian, F. Hosseinzadeh, C. Migneco, M.V.L. Fook, F. Baino, Bioceramic coatings on metallic implants: an overview, Ceram. Int. 48 (2022) 8987–9005, https://doi.org/10.1016/j.ceramint.2022.02.055.

[12] M. Rahmati, M. Mozafar, Biocompatibility of alumina-based biomaterials–a review, J. Cell. Physiol. 234 (2018) 3321–3335, https://doi.org/10.1002/jcp.27292.

[13] V. Vishwakarma, G.S. Kaliaraj, K.K.A. Mosas, Multifunctional coatings on implant materials - a systematic review of the current scenario, Coatings 13 (2023) 69–86, https://doi.org/10.3390/coatings13010069.

[14] C. Piconi, A.A. Porporati, Bioinert Ceramics: zirconia and Alumina, in: I. Antoniac (Ed.), Handbook of Bioceramics and Biocomposites, Springer, Cham., 2016, pp. 58–89, https://doi.org/10.1007/978-3-319-12460-5_4.

[15] R.J. Damani, D. Rubeša, R. Danzer, Fracture toughness, strength and thermal shock behaviour of bulk plasma sprayed alumina - effects of heat treatment, J. Eur. Ceram. Soc. 20 (2000) 1439–1452, https://doi.org/10.1016/S0955-2219(00)00033-9.

[16] M. Michalak, P. Sokołowski, M. Szala, M. Walczak, L. Łatka, F. Toma, S. Björklund, Wear behavior analysis of Al₂O₃ coatings manufactured by APS and HVOF spraying processes using powder and suspension feedstocks, Coat 11 (2021) 879, https://doi.org/10.3390/coatings11080879.

[17] K.A. Habib, J.J. Saura, C. Ferrer, M.S. Damra, E. Giménez, L. Cabedo, Comparison of flame sprayed Al₂O₃/TiO₂ coatings: their microstructure, mechanical properties and tribology behavior, Surf. Coat. Int. 201 (2006) 1436–1443, https://doi.org/10.1016/j.surfcoat.2006.02.011.

[18] M.J. Ghazali, S.M. Forghani, N. Hassanuddin, A. Muchtar, A.R. Daud, Comparative wear study of plasma sprayed TiO₂ and Al₂O₃–TiO₂ on mild steels, Tribol. Int. 93 (2016) 681–686, https://doi.org/10.1016/j.triboint.2015.05.001.

[19] A.M. Limargaa, S. Widjajab, T.H. Yip, Mechanical properties and oxidation resistance of plasma-sprayed multilayered Al₂O₃/ZrO₂ thermal barrier coatings, Surf. Coat. Technol. 197 (2005) 93–102, https://doi.org/10.1016/j.surfcoat.2005.02.087.

[20] J. Kiilakoski, R. Musalek, F. Lukac, H. Koivuluoto, P. Vuoristo, Evaluating the toughness of APS and HVOF-sprayed Al₂O₃-ZrO₂-coatings by in-situ- and macroscopic bending, J. Eur. Ceram. Soc. 38 (2018) 1908–1918, https://doi.org/10.1016/j.jeurceramsoc.2017.11.056.

[21] P. Gao, Y. Ma, W. Sun, Y. Yang, C. Zhang, Y. Cui, Y. Wang, Y. Dong, Microstructure and properties of Al₂O₃–ZrO₂–TiO₂ composite coatings prepared by plasma spraying, Rare Met 40 (2021) 1825–1834, https://doi.org/10.1007/s12598-020-01505-2.

[22] Y. Ma, X. Wang, X. Sun, Y. Yang, C. Zhang, P. Gao, Y. Cui, L. Wang, Y. Dong, Y. Wang, Microstructure and properties evolution of plasma sprayed Al₂O₃-ZrO₂-TiO₂ coatings during high temperature and thermal shock resistance, Mater. High Temp 37 (2020) 256–267, https://doi.org/10.1016/j.jre.2020.09.008.

[23] D. Tejero-Martin, M. Rezvani Rad, A. McDonald, T. Hussain, Beyond traditional coatings: a review on thermal-sprayed functional and smart coatings, J. Therm. Spray Technol. 28 (2019) 598–644, https://doi.org/10.1007/s11666-019-00857-1.

[24] S. Singh, C.C. Berndt, R.K. Singh Raman, H. Singhand A. S. M. Ang, Applications and Developments of Thermal Spray Coatings for the Iron and Steel Industry, Mater 16 (2023) 516, https://doi.org/10.3390/ma16020516.

[25] R.B. Heimann, Plasma-spray coating: Principles and Applications, VCH, Weinheim, 2008.

[26] F. Miranda, F. Caliari, A. Essiptchouk, G. Petraconi, Atmospheric plasma spray processes: from micro to nanostructures, in: A. Nikiforov, Z. Chen (Eds.), Atmospheric Pressure Plasma – from Diagnostics to Applications, IntechOpen, London, 2019, pp. 97–109.

[27] J.L. Dorier, M. Gindrat, C. Hollenstein, A. Salito, M. Loch, G. Barbezat, Time-resolved imaging of anodic arc root behavior during fluctuations of a DC plasma spraying torch, IEEE TPS 29 (2001) 494–501, https://doi.org/10.1109/27.928947.

[28] S. Liu, J.P. Trelles, C. Li, C. Li, H. Guo, A review and progress of multiphase flows in atmospheric and low-pressure plasma spray advanced coating, Mater. Today Phys. 27 (2002) 100832, https://doi.org/10.1016/j.mtphys.2022.100832.

[29] G. Darut, M. Planche; H. Liao; C. Adam; A. Salito and M. Rösli, Study of the in-flight characteristics of particles for different configurations of cascade plasma torches, Proc. Int. Therm. Spray Conf. (2021) 499–507. https://doi.org/10.31399/asm.cp.itsc2021p0499.

[30] G. Darut, M. Planche, R. Seulin, C. Adam, H. Liao, J.J. Gonzalez, P. Freton, A. Salito, M. Rösli, Complementary studies (measures and modelling) on the running of cascade plasma torch applied on zirconia coatings, in: Proc. Int. Therm. Spray Conf, 2023.

[31] O.P. Solonenko, A.V. Smirnov, Advanced oxide powders processing based on cascade plasma, J. Phys.: Conf. Ser. 550 (2014) 012017, https://doi.org/10.1088/1742-6596/550/1/012017.

[32] R. Chidambaram Seshadri, S. Sampath, Characteristics of conventional and cascaded arc plasma spray-deposited ceramic under standard and high-throughput conditions, J. Therm. Spray. Tech. 28 (2019) 690–705, https://doi.org/10.1007/s11666-019-00841-9.

[33] M. Herbster, J. Döring, J. Nohava, C.H. Lohmann T. Halle, J. Bertrand, Retrieval study of commercially available knee implant coatings TiN, TiNbN and ZrN on TiAl6V4 and CoCr28Mo6, J. Mech. Behav. Biomed. Mater. 112 (2020) 104034, https://doi.org/10.1016/j.jmbbm.2020.104034.

[34] X. Wu, H. Han, Y. Jiang, D. Zhu, B. Zuo, S. Bian, C. Chen, L. Zhao, J. Xu, L. Yu, Opportunities and challenges of the nitride coatings for artificial implants: a review, Surf. Coat. 480 (2024) 130587, https://doi.org/10.1016/j.surfcoat.2024.130587.

[35] T. Weitkamp, P. Tafforeau; E. Boller; P. Cloetens; J. Valade; P. Bernard, F. Peyrin, W. Ludwig, L. Helfen and J. Baruchel, Status and evolution of the ESRF beamline ID19, AIP Conf. Proc. (2010) 1221: 33–38. https://doi.org/10.1063/1.3399253.

[36] A. Hermann, et al., Understanding indentation, scratch and wear behavior of UV-cured wood finishing products, Prog. Org. Coat. 161 (2021) 106504, https://doi.org/10.1016/j.porgcoat.2021.106504.

[37] L. Helfen, T. Baumbach, P. Mikulík, D. Kiel, P. Pernot, P. Cloetens, J. Baruchel, High-resolution three-dimensional imaging of flat objects by synchrotron-radiation computed laminography, Appl. Phys. Lett. 86 (2005) 071915, https://doi.org/10.1063/1.1854735.

[38] L. Helfen, A. Myagotin, P. Mikulík, P. Pernot, A. Voropaev, M. Elyyan, M. Di Michiel, J. Baruchel, T. Baumbach, On the implementation of computed laminography using synchrotron radiation, Rev. Sci. Instrum. 82 (2011) 063702, https://doi.org/10.1063/1.3596566.

[39] M. Klinger, More features, more tools, more CrysTBox, J. Appl. Crystallogr. 50 (4) (2017), https://doi.org/10.1107/S1600576717006793.

[40] D. Wu, J. San, F. Niu, D. Zhao, Y. Huang, G. Ma, Directed laser deposition of Al₂O₃–ZrO₂ melt-grown composite ceramics with multiple composition ratios, J. Mater. Sci. 55 (2020) 6794–6809, https://doi.org/10.1007/s10853-020-04524-7.

[41] Y. Xia, J. Mou, G. Deng, S. Wan, K. Tieu, H. Zhu, Q. Xue, Sintered ZrO₂–TiO₂ ceramic composite and its mechanical appraisal, Ceram. Int. 46 (2020) 775–785, https://doi.org/10.1016/j.ceramint.2019.09.032.

[42] H. Manshor, S. Md Aris, A.Z.A. Azhar, E.C. Abdullah, Z. Ahmad, Effects of TiO₂ addition on the phase, mechanical properties, and microstructure of zirconia-toughened alumina ceramic composite, Ceram. Int. 41 (2015) 3961–3967, https://doi.org/10.1016/j.ceramint.2014.11.080.